



Research paper

Model-based optimal design of phase change ionic liquids for efficient thermal energy storage

Huaiwei Shi ^a, Xiang Zhang ^b, Kai Sundmacher ^{a,b}, Teng Zhou ^{a,b,*}

^a Process Systems Engineering, Otto-von-Guericke University Magdeburg, Universitätsplatz 2, Magdeburg, D-39106, Germany

^b Process Systems Engineering, Max Planck Institute for Dynamics of Complex Technical Systems, Sandtorstr. 1, Magdeburg, D-39106, Germany

Received 26 October 2020; revised 16 December 2020; accepted 22 December 2020

Available online 26 December 2020

Abstract

The selection of phase change material (PCM) plays an important role in developing high-efficient thermal energy storage (TES) processes. Ionic liquids (ILs) or organic salts are thermally stable, non-volatile, and non-flammable. Importantly, researchers have proved that some ILs possess higher latent heat of fusion than conventional PCMs. Despite these attractive characteristics, yet surprisingly, little research has been performed to the systematic selection or structural design of ILs for TES. Besides, most of the existing work is only focused on the latent heat when selecting PCMs. However, one should note that other properties such as heat capacity and thermal conductivity could affect the TES performance as well. In this work, we propose a computer-aided molecular design (CAMD) based method to systematically design IL PCMs for a practical TES process. The effects of different IL properties are simultaneously captured in the IL property models and TES process models. Optimal ILs holding a best compromise of all the properties are identified through the solution of a formulated CAMD problem where the TES performance of the process is maximized. [MPyEtOH][TfO] is found to be the best material and excitingly, the identified top nine ILs all show a higher TES performance than the traditional PCM paraffin wax at 10 h thermal charging time.

© 2020, Institute of Process Engineering, Chinese Academy of Sciences. Publishing services by Elsevier B.V. on behalf of KeAi Communications Co., Ltd. This is an open access article under the CC BY-NC-ND license (<http://creativecommons.org/licenses/by-nc-nd/4.0/>).

Keywords: Ionic liquid; Phase change material; Thermal energy storage; Computer-aided molecular design; Process modelling and evaluation

1. Introduction

Thermal energy (e.g., solar radiation and industrial waste heat) is widely available and easy to access. It can be stored in the form of latent heat, sensible heat, or both. In comparison with sensible heat storage (SHS), latent heat storage (LHS) is more attractive due to its much higher energy density with smaller temperature change [1,2]. Typically, LHS can be accomplished through solid–liquid and liquid–gas phase transformations. The solid–liquid transformation has been proven to be more attractive for use in large-scale thermal energy storage (TES) due to its small volume changes during

phase transition. In such a system, a phase change material (PCM) absorbs heat from a high-temperature heat transfer fluid (HTF) and melts; and the PCM releases heat to the cold HTF when it solidifies.

The selection of PCM plays an important role in developing high-efficient TES system. A suitable melting point that matches the specific application is the prerequisite for selecting PCMs. For example, materials with a low melting point (below 5 °C) can be used for food refrigerator [3]. PCMs with a medium melting temperature is suitable for solar hot-water generation [4] and PCM with an even higher melting point can be used for solar thermal power plant and industrial waste heat recovery [5,6]. Besides a suitable melting point, PCMs must exhibit other desirable properties, such as a high thermal conductivity and heat of fusion as well as a low viscosity and corrosivity [7]. Organic PCMs feature moderate melting point,

* Corresponding author. Process Systems Engineering, Otto-von-Guericke University Magdeburg, Universitätsplatz 2, Magdeburg, D-39106, Germany.
E-mail address: zhout@mpi-magdeburg.mpg.de (T. Zhou).

making them suitable for a wide range of applications. However, their thermal conductivity and density is generally quite low. Besides, they are usually volatile and flammable [8]. Inorganic salts usually possess a high thermal conductivity. However, they have an extremely high melting temperature (for example, T_m of NaCl is 801 °C) and suffer from corrosion and supercooling [9]. These drawbacks of the conventional PCMs promote the development of new high-performing TES materials.

Ionic liquids (ILs), or known as organic salts, are composed of organic cations and organic or inorganic anions. This new type of material is thermally stable, non-volatile, and nonflammable. Importantly, their properties can be well tuned by changing the cation, anion, and/or the substituent groups [10–16]. It was demonstrated that a well-selected IL could possess a higher heat of fusion than the commercial PCMs whose heat of fusion are around 100 J g⁻¹ [17,18]. For example, Zhu et al. [18] reported the heat of fusion for a family of alkylimidazolium bromide ILs and demonstrated that [C₁₆mim]Br has the largest heat of fusion 153 J g⁻¹. Vijayraghavan et al. [19] investigated a series of protic organic salts and found that their heat of fusion are as high as 190 J g⁻¹. Here, we would like to mention that even though ILs are commonly known to be liquid at or near room temperature, the official definition of ILs is not like this. Instead, ILs are defined as organic salts with melting points below 100 °C [20]. The wide range of melting temperature spanning from negative up to 100 °C and the large ability to tailor the properties make ILs promising, designable heat storage materials.

Until now, most of the existing work is focused on the heat of fusion when selecting PCMs. However, one should note that in reality, rarely are these materials being used only during the phase change period. In fact, LHS is always combined with SHS. In this context, in addition to melting point and latent heat, heat capacity is also essential for selecting PCMs. Moreover, thermal conductivity needs to be considered as well because it can largely affect the heat transfer rate. The impact of all these properties can be captured only when a real TES process is modelled and evaluated.

In this contribution, a computer-aided molecular design (CAMD) [21–24] based method is proposed to systematically design phase change ILs (PCILs) for a practical TES process. Detailed mathematical models are introduced for this process and a performance index is defined to represent the TES performance of the employed PCIL. Later, group contribution (GC) models are developed and used to predict key IL properties (latent heat, melting point, heat capacity, etc.) that affect the process performance. Combining these GC-based property models with the TES process models, an optimization problem is finally formulated to maximize the performance index function. After solving the problem, optimal ILs achieving a best compromise of all the different properties are identified. In order to demonstrate the advantage of model-based material design, the TES performance of the identified ILs is compared with that of a benchmark PCM paraffin wax.

2. Task description

In order to increase the heat transfer area between the HTF and PCM, PCM is usually encapsulated by, for example stainless steel or thermally stable polymer, to form spherical capsules. These capsules are then packed into a heat storage tank where the HTF flows in and out when exchanging heat. Such a TES system is governed by a set of heat balance relations in the form of partial differential equations (PDEs). Fig. 1 shows the schematic diagram of the investigated TES system. The cylindrical TES tank is made of steel with 1.0 m diameter ($D = 1.0$ m) and 1.52 m length ($l = 1.52$ m), filled with spherical PCM capsules whose diameters are 0.04 m. Water is used as the high-temperature HTF to provide heat to the PCM. The HTF flows through the tank with a mass flow rate $\dot{m} = 0.0796$ kg s⁻¹. The heat capacity ($C_{p,f}$), thermal conductivity (λ_f), viscosity (μ_f) and density (ρ_f) of water are 4188.5 J kg⁻¹ K⁻¹, 0.662 W m⁻¹ K⁻¹, 0.000434 Pa s and 998 kg m⁻³, respectively. Before starting, all the PCMs in the tank have the same temperature of 323.15 K. The space between PCM capsules are already filled with water at the same temperature. When the thermal charging process starts, hot water at 343.15 K flows into the tank from the top. PCM, which is initially at solid state, starts to absorb heat and melt when the temperature reaches its melting point. The charging process is completely finished when all the PCMs reach 343.15 K. However, this process can be terminated earlier because the charging rate is decreasing over time. Besides, the total thermal charging time also depends on the duration of sunshine that generates the hot water. The objective is to identify optimal PCILs for this specific TES system.

3. Process modelling

In order to evaluate the TES performance of a PCIL in the thermal storage process (Fig. 1), two different types of models

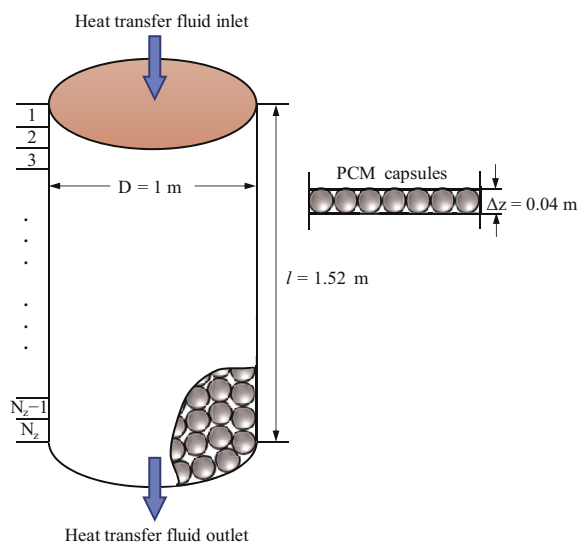


Fig. 1. Layout and details of the thermal storage tank.

are required. They are property models that link IL structure to its thermo-physical properties and process models that predict the TES performance of the process using the IL properties as inputs. In this section, we first present the detailed mathematical models for the investigated TES process. The model is later validated by comparing our simulation results with the literature results. In the next section, GC-based property models are introduced to predict IL properties.

Before deriving the governing equations for the TES system, some reasonable assumptions need to be stated. It is assumed that the HTF water has a one-dimensional axial flow and temperature distribution. Only heat convection is considered in this flow direction. For the PCM spheres, one-dimensional radial heat conduction is considered. The density, heat capacity and thermal conductivity of PCM are constant during the whole TES process. Heat conduction between different spheres are neglected. The ambient heat losses and radiation heat transfer are also neglected.

As shown in Fig. 1, the cylindrical tank is discretized into 38 equal sections ($N_z = 38$) in the fluid flow direction, where the fluid temperature within each section is assumed to be a constant. The height of each section equals to 0.04 m, making one tank section containing exactly a single layer of PCM capsules. The entire PCM capsules are discretized into 13 control volumes ($N_r = 14$) along the radial direction, as illustrated in Fig. 2. Note that the inner surface of PCM capsules is indicated when the discretization index equals ($N_r - 1$). The discretization index of N_r represents the position where the HTF locates. As one-dimensional radial heat conduction is considered, all the PCM in the same tank section has the same temperature distribution inside the capsules. Therefore, only one sphere per tank section is simulated.

3.1. Model equations

The heat balance equation for the fluid is written as Eq. (1) where the left-hand term is the heat accumulation of the fluid

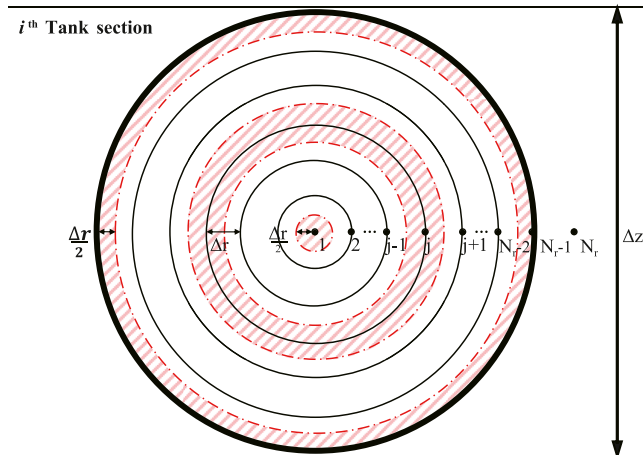


Fig. 2. Discretization details of the PCM sphere (regions filled with red slash are control volumes).

in the i -th tank section and the first term on the right side is the heat convection of the fluid. The second term on the right side indicates the heat transferred from the fluid to the inner surface of the PCM capsule.

$$\rho_f V_{i,f} C_{p,f} \frac{\partial T_{i,f}}{\partial t} = \dot{m} C_{p,f} (T_{i,f}^{in} - T_{i,f}^{out}) - n_{i,cap} \frac{T_{i,f} - T_{i,N_r-1}}{R_{total}} \quad (\text{for } 1 \leq i \leq N_z) \quad (1)$$

Because $j = N_r$ denotes the position of the fluid, its temperature $T_{i,f}$ can be re-written into T_{i,N_r} . ρ_f and $C_{p,f}$ are the density and specific heat capacity of the fluid. The subscript i indicates the i -th tank section where water temperature $T_{i,f}$ is being calculated. $V_{i,f}$ is the volume of water in the i -th tank section. \dot{m} represents the mass flow rate of the fluid. $T_{i,f}^{out}$ and $T_{i,f}^{in}$ are the temperatures of the outlet and inlet fluid to the i -th tank section. T_{i,N_r-1} is the temperature of the inner surface of the capsule shell. R_{total} is the total thermal resistance between the fluid and the inner surface of the capsule shell, which is calculated from Eqs. (7)–(10).

$$\Delta z = \frac{l}{N_z} = \frac{1.52 \text{ m}}{38} = 0.04 \text{ m} \quad (2)$$

$$V_{i,f} = \pi \left(\frac{D}{2} \right)^2 \Delta z \epsilon \quad (3)$$

$$V_{i,cap} = \pi \left(\frac{D}{2} \right)^2 \Delta z (1 - \epsilon) \quad (4)$$

$$n_{i,cap} = \frac{V_{i,cap}}{\frac{4\pi}{3} r_{cap-ext}^3} \quad (5)$$

$$A_{cap-ext} = 4\pi (r_{cap-ext})^2 \quad (6)$$

Δz is the discretization interval in the axial direction. $V_{i,cap}$ is the volume of PCM capsules in the i -th tank section with a porosity $\epsilon = 0.4$ [25]. $n_{i,cap}$ is the number of capsules in the i -th section and $A_{cap-ext}$ is the external area of a PCM capsule. The external radius of the capsule $r_{cap-ext}$ is 0.02 m.

$$R_{total} = R_{conv} + R_{cond} \quad (7)$$

$$R_{conv} = \frac{1}{h_f A_{cap-ext}} \quad (8)$$

$$R_{cond} = \frac{\left(\frac{1}{r_{cap-int}} - \frac{1}{r_{cap-ext}} \right)}{4\pi \lambda_{shell}} \quad (9)$$

$$h_f = \frac{\lambda_f \cdot Nu}{D_{cap-ext}} \quad (10)$$

R_{conv} and R_{cond} are the thermal resistance of heat convection between the fluid and the external surface of capsule shell and the thermal resistance of heat conduction through the capsule shell, respectively. $r_{cap-int}$ is the internal radius of the capsule

($r_{cap-int} = r_{cap-ext} - w$). The shell thickness w is 0.0004 m. λ_{shell} and λ_f are the thermal conductivity of the shell and the fluid, respectively. Stainless steel is used as the shell material whose λ_{shell} is 14.4 W m⁻¹ K⁻¹. h_f is the heat transfer coefficient between the fluid and capsules [26] and $D_{cap-ext}$ indicates the external diameter of the capsule (0.04 m). Nu is the Nusselt number that can be obtained from Eqs. (11)–(15).

$$Nu = 2.0 + 1.1Re^{0.6}Pr^{0.333}, \text{ When } 15 < Re < 8500; [27](11)$$

$$Nu = 18.1Pr^{0.333}, \text{ When } Re < 40; [28] \quad (12)$$

$$Re = \frac{\dot{m}}{A_{cro-f}} \frac{D_{cap-ext}}{\mu_f}; [26] \quad (13)$$

$$A_{cro-f} = \pi \left(\frac{D}{2} \right)^2 \cdot \epsilon \quad (14)$$

$$Pr = \frac{C_{p,f} \cdot \mu_f}{\lambda_f} \quad (15)$$

Re denotes the Reynolds number and Pr denotes the Prandtl number. A_{cro-f} is the average cross-sectional area of the flowing fluid, which is the product of the porosity and the cross-sectional area of the tank. μ_f is the dynamic viscosity of the fluid. Since the validity ranges of Eq. (11) and Eq. (12) are partially overlapped, the higher Nusselt number is selected when two different Nu values are obtained [26].

The temperature of PCM follows the spherical heat conduction equation.

$$\rho \left(\frac{\partial H}{\partial t} \right)_{ij} = \frac{2\lambda}{r_{ij}} \left(\frac{\partial T}{\partial r} \right)_{ij} + \lambda \left(\frac{\partial^2 T}{\partial r^2} \right)_{ij} \quad (\text{for } 1 \leq i \leq N_z \text{ and } 1 < j < N_r - 1) \quad (16)$$

Due to the limited difference between liquid and solid PCM properties, the heat capacity, thermal conductivity, and density of the liquid and solid PCM are assumed the same. Under this condition, even though the solid–liquid interface moves all the time during the melting process, the same equation (Eq. (16)) with the same property parameters can be used to describe the static heat conduction in both solid and liquid sides.

Two boundary conditions are:

$$\rho V_{i,1} \left(\frac{\partial H}{\partial t} \right)_{i,1} = \lambda \left(A \frac{\partial T}{\partial r} \right)_{i, \frac{1}{2}} \quad (\text{for } 1 \leq i \leq N_z \text{ and } j = 1) \quad (17)$$

$$\rho V_{i,N_r-1} \left(\frac{\partial H}{\partial t} \right)_{i,N_r-1} = \frac{T_{i,f} - T_{i,N_r-1}}{R_{total}} - \lambda \left(A \frac{\partial T}{\partial r} \right)_{i,N_r-\frac{3}{2}} \quad (\text{for } 1 \leq i \leq N_z \text{ and } j = N_r - 1) \quad (18)$$

Where ρ and λ are the density and thermal conductivity of PCM, respectively. H and T are the specific enthalpy and

temperature of the PCM, respectively. r indicates the radius of the PCM capsule. As shown in Fig. 2, $V_{i,1}$ and V_{i,N_r-1} are the volumes of the first and last control volumes in the sphere radial direction. $A_{i,1}$ and A_{i,N_r-1} are the corresponding surface areas of them.

$$V_{i,1} = \frac{4}{3} \pi \left(\frac{\Delta r}{2} \right)^3 = \frac{1}{6} \pi (\Delta r)^3 \quad (19)$$

$$A_{i,\frac{3}{2}} = 4\pi \left(\frac{\Delta r}{2} \right)^2 = \pi (\Delta r)^2 \quad (20)$$

$$V_{i,N_r-1} = \frac{4}{3} \pi \left[(12\Delta r)^3 - \left(12\Delta r - \frac{\Delta r}{2} \right)^3 \right] = \frac{1657}{6} \pi (\Delta r)^3 \quad (21)$$

$$A_{i,N_r-\frac{3}{2}} = 4\pi \left(12\Delta r - \frac{\Delta r}{2} \right)^2 = 529\pi (\Delta r)^2 \quad (22)$$

where

$$\Delta r = \frac{r_{cap-ext} - w}{N_r - 2} = 0.00163 \text{ m} \quad (23)$$

To solve Eqs. (16)–(18), it is necessary to define a relation between the enthalpy and temperature of the PCM. For a constant phase-change temperature, the enthalpy and temperature relation is defined by the following equations.

$$H = C_p T \text{ when } T < T_m \quad (24)$$

$$C_p T_m \leq H \leq C_p T_m + L \text{ when } T = T_m \quad (25)$$

$$H = C_p T + L \text{ when } T > T_m \quad (26)$$

where C_p , T_m , and L represent the heat capacity, melting temperature, and latent heat of the PCM. It is clear that in total five PCM properties are used in the above model equations. They are ρ , λ , C_p , T_m , and L .

Following the upwind-like scheme ($T_{i,f}^{in} - T_{i,f}^{out}$) is written as ($T_{i-1,f} - T_{i,f}$) and further re-expressed into ($T_{i-1,N_r} - T_{i,N_r}$). The explicit difference method is used to discretize Eq. (1) and Eqs. (16)–(18). The initial PCM temperatures $T_{i,j}^0$ are 323.15 K ($1 \leq i \leq N_z$ and $1 \leq j \leq N_r - 1$) and the initial temperature of

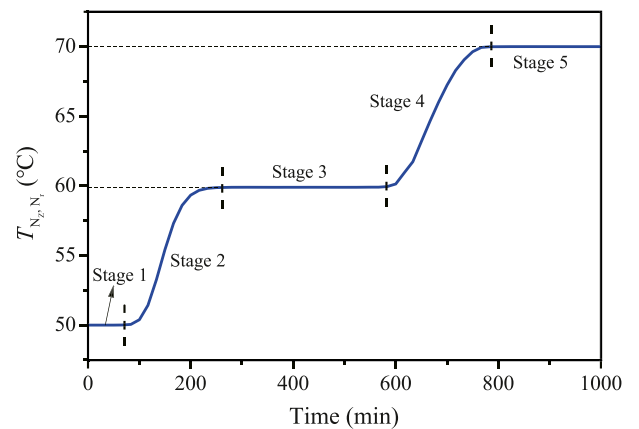


Fig. 3. Evolution of outlet water temperature during the thermal charging process.

the fluid inside the tank T_{i,N_r}^0 is also 323.15 K. Moreover, at any time during the thermal charging process, the inlet fluid temperature T_{0,N_r}^t is 343.15 K ($0 \leq t \leq t_{\text{end}}$). Based on these initial conditions and the enthalpy–temperature relations, the PCM temperature distribution inside the capsules and temperature profile of the fluid along the tank can be obtained by solving the discretized algebraic equations.

3.2. Model validation

The process model described above is validated in this section by comparing the simulated results with those from Galione et al. [26] where paraffin wax # 60 is used as the PCM. It has the following properties: $\rho = 850 \text{ kg m}^{-3}$, $C_p = 2150 \text{ J kg}^{-1} \text{ K}^{-1}$, $\lambda = 0.230 \text{ W m}^{-1} \text{ K}^{-1}$, $L = 190,000 \text{ J kg}^{-1}$, $T_m = 333.05 \text{ K}$.

Fig. 3 presents the evolution of the outlet water temperature (i.e., T_{N_z,N_r}) over the thermal charging time. As illustrated, the whole charging period can be divided into 5 different stages. In Stage 1, it takes about 68 min to warm up all the PCM capsules until the lowermost PCMs get heat. During this period, a constant outlet water temperature of 323.15 K is observed. In Stage 2 (68 min–265 min), an increasing of outlet water temperature is observed due to the sensible heat absorption and temperature increase of the PCMs at the bottom of the tank. In Stage 3 (till 583 min) when the LHS of the bottom PCMs takes place, the outlet water temperature stays at the melting point of the wax (i.e., 59.9 °C) until all the lowermost PCM capsules are completely melted. Next, in Stage 4 till 785 min, the outlet water temperature starts to increase again because the melted

bottom PCMs start SHS again. Finally in Stage 5, the temperature of all the PCM capsules reaches the inlet water temperature (70 °C), indicating that the TES process is completed.

In order to illustrate the different stages in a more vivid way, Fig. 4 shows the temperature distribution of the PCM and water (rightmost of each color column) at different stages of the charging process. It is found that our simulation results are consistent with those obtained in Ref. [26]. This demonstrates that the model we used is correct and the employed discretization method is reliable.

3.3. System performance evaluation

After the successful validation of the model, a performance index function is defined to evaluate the TES performance of the system. Here, we use the thermal storage power as the performance indicator to design the best PCIL for this system. It should be noted that the thermal storage power is not a constant during the charging process. In the beginning, heat transfer is fast because the temperature gradient between PCM and water is high. The thermal storage power decreases gradually as the PCM temperature gets closer to the fluid temperature. Therefore, an average thermal storage power, defined as the total absorbed heat over the thermal charging time, is used to represent the overall TES performance of the system or the material. Unfortunately, it is complicated to quantify the total absorbed heat from PCM due to the temperature distribution inside the capsules. Here, we calculate this energy from the heat provided by water, as indicated by Eq. (1).

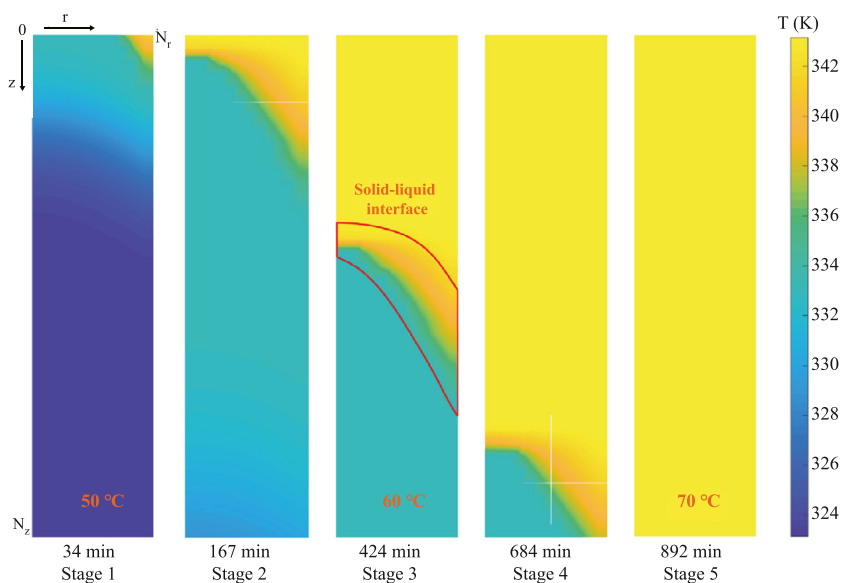


Fig. 4. Evolution of the temperature of PCM and water during the thermal charging process.

$$E = \sum_{t=0}^{t_{end}} \sum_{i=1}^{N_z} \left(\dot{m} C_{p,f} (T_{i-1,f}^t - T_{i,f}^t) - \rho_f V_{i,f} C_{p,f} \left(\frac{T_{i,f}^{t+\Delta t} - T_{i,f}^t}{\Delta t} \right) \right) \quad (27)$$

E is the total energy provided by water to the PCMs. The selected discretization time step $\Delta t = 1.0$ s. Now, the average TES power of the system at an arbitrary thermal charging time t_{end} can be quantified by Eq. (28).

$$POW = E/t_{end} \quad (28)$$

4. Property modelling

As clearly indicated by the process models, five thermo-physical properties (ρ , λ , C_p , T_m , and L) of PCM are required to quantify the TES performance of the material. GC-based methods are the most widely used class of property estimation methods in CAMD due to their easy incorporation within mathematical models/optimizations and high qualitatively correct estimations. After a careful literature review, we found that there are already existing GC models for predicting the density, thermal conductivity, heat capacity and melting point of ILs. However, until now no GC model has been reported for estimating the latent heat of ILs. Therefore, in this section, a GC-based IL latent heat prediction model is first developed. Later, we summarize the existing GC models for the other four properties.

4.1. Latent heat of fusion

Experimental heat of fusion data are collected from the IL Thermo Database [29]. For obtaining reliable model, data with an uncertainty higher than 10% are removed. If more than one heat of fusion data are available for a specific IL, the inconsistent data are also removed after checking the consistency, for example, by analogizing the latent heat of similar structures. Finally, a total number of 161 data points for 111 different ILs are collected.

$$L = C + \sum_k n_k \Delta l_k \quad (29)$$

In Eq. (29), L with a unit of kJ mol^{-1} represents the latent heat of IL, C is a fitting constant, n_k is the number of occurrences of group k present in the IL molecule, and Δl_k is the value of the contribution of the k -th group to the latent heat. The constant C and group contributions are obtained by data regression, more specifically, by minimizing the summation of the deviations between the experimental and calculated latent heat. To build the GC model, IL molecules must be decomposed into separate building groups in advance. In this work, 59 different groups are identified where the cation core and anion is treated as a whole group. The abbreviations, detailed structures, and Δl_k of the 59 groups are summarized in the Supporting Information. The regressed latent heat model is given below.

$$L = 17.26 + \sum_{k=1}^{59} n_k \Delta l_k \quad (30)$$

The performance of the above model is evaluated by R-square (R^2) and the average absolute relative deviation (AARD) between the experimental and calculated latent heat.

$$R^2 = 1 - \frac{\sum_{i=1}^N (L_i^{\text{exp}} - L_i^{\text{cal}})^2}{\sum_{i=1}^N \left(L_i^{\text{exp}} - \frac{1}{N} \sum_{i=1}^N L_i^{\text{exp}} \right)^2} \quad (31)$$

$$AARD = \frac{1}{N} \cdot \sum_{i=1}^N \frac{|L_i^{\text{exp}} - L_i^{\text{cal}}|}{L_i^{\text{exp}}} \quad (32)$$

The comparison of calculated and experimental latent heat of ILs is shown in Fig. 5. It is seen that most of the points distribute around the diagonal line except for a small proportion of outliers. The determined AARD and R^2 between the calculated and experimental data are 16.9% and 0.8427. The comparison plot together with the estimated performance statistics indicate that the developed GC model can give a satisfying prediction on the latent heat of ILs.

4.2. Density, heat capacity and thermal conductivity

Huang et al. [30] proposed a Fragment Contribution-Corresponding States (FC-CS) method to predict physicochemical properties of ILs. The main equations are given below.

$$M = \sum_k n_k \Delta M_k \quad (33)$$

$$T_b = 198.2 + \sum_k n_k \Delta T_{b,k} \quad (34)$$

$$T_c = \frac{T_b}{0.5703 + 1.0121 \sum_k n_k \Delta T_{c,k} - (\sum_k n_k \Delta T_{c,k})^2} \quad (35)$$

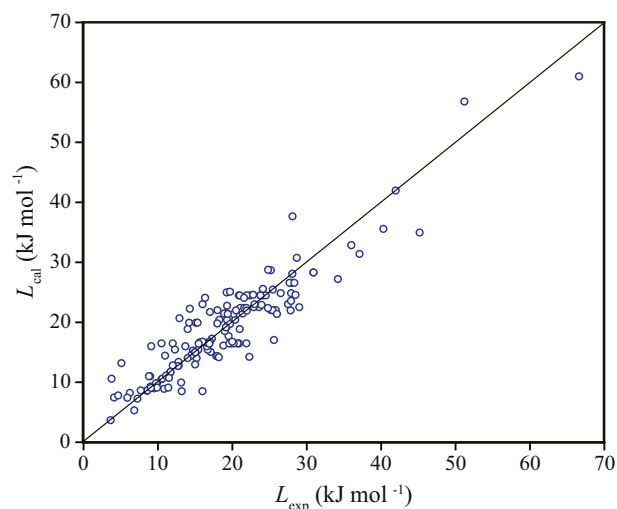


Fig. 5. Comparison between experimental and model-calculated latent heat of ILs.

$$P_c = \frac{M}{(0.34 + \sum_k n_k \Delta P_{c,k})^2} \quad (36)$$

$$V_c = 28.8946 + 14.75246 \sum_k n_k \Delta V_{c,k} + \frac{6.03853}{\sum_k n_k \Delta V_{c,k}} \quad (37)$$

$$\omega = \frac{T_b T_c}{(T_c - T_b)(0.7 T_c)} \log_{10} \left(\frac{P_c}{P_b} \right) - \left(\frac{T_c}{T_c - T_b} \right) \log_{10} \left(\frac{P_c}{P_b} \right) + \log_{10} \left(\frac{P_c}{P_b} \right) - 1 \quad (38)$$

n_k represents the number of group k appearing in the IL molecule. ΔM_k , $\Delta T_{b,k}$, $\Delta T_{c,k}$, $\Delta P_{c,k}$, and $\Delta V_{c,k}$ denote the contribution of group k to the molecular weight, boiling temperature, critical temperature, critical pressure, and critical volume of IL, respectively. P_b is the atmospheric pressure in bar (1.013 bar).

IL density, heat capacity, and thermal conductivity are quantified by Eqs. (39)–(41) where T_r is the reduced temperature ($T_r = T/T_c$) and T_{br} is the reduced temperature at the normal boiling point ($T_{br} = T_b/T_c$).

$$\rho = \frac{M}{V_c} [1 + 0.85(1 - T_r) + (1.6916 + 0.984\omega)(1 - T_r)^{1/3}] \quad (39)$$

$$C_p = M\omega T_c^{1.565} T_c^{0.15} \left[\left(\frac{1 - T_{br}}{1 + T_r} \right)^{4.126} - 0.00005 \right] / P_c^{0.7568} \quad (40)$$

$$\lambda = \left(\frac{11.1}{T_c^{1.091}} + \frac{0.6107 T_{br}^{0.552}}{0.1369 M^{0.5817}} \right) \left[1 - 0.007 \left(\frac{P}{P_c} \right)^{0.7} \right] \quad (41)$$

According to Huang et al. [30], for the collected experimental property data, the overall AARD for IL density, heat capacity, and thermal conductivity are 3.3%, 3.8%, and 3.5%, respectively. Due to the small variation range of temperature in the thermal charging process, it is assumed that these properties keep unchanged during the whole process.

It should be noted that the groups or fragments used in Huang et al. [30] are inconsistent with the group set defined in the latent heat prediction. Fortunately, it is possible to derive the contributions of new groups based on the additivity characteristic of GC methods. Thus, the fragments defined in Huang et al. [30] are integrated and transformed into the groups used for latent heat prediction. The resulting new contribution values (ΔM_k , $\Delta T_{b,k}$, $\Delta T_{c,k}$, $\Delta P_{c,k}$, and $\Delta V_{c,k}$) of the 59 groups are provided in the Supporting Information.

4.3. Melting point

In the literature, there are a large number of analytical expressions that allow the prediction of the melting point for diverse substances [31,32]. Here, we choose a simple GC-based model [33] to predict IL melting point due to its easy integration into the CAMD framework. In Ref. [33],

experimental melting points for a set of 200 diverse ILs are collected and used to regress the contributions of IL building groups. It was proven that the established GC model is an excellent alternative for the estimation of the melting point of ILs, with an average deviation of 7%. Note that the IL groups defined in Ref. [33] are not exactly the same with the groups that are used for the heat of fusion prediction. Similarly, the GC model developed in Ref. [33] is converted for our use by adding the contributions of groups. Eq. (42) provides the mathematical expression of the GC model and the final group contribution values $\Delta T_{m,k}$ are summarized in the Supporting Information.

$$T_m = 288.7 + \sum_{k=1}^{59} n_k \Delta T_{m,k} \quad (42)$$

5. Computer-aided IL design

Computer-aided molecular design (CAMD) is a systematic method for designing molecules that possess certain desirable properties. It has been widely used in the optimal design of IL solvents for various applications [22,24,34–39]. Typically, IL structural and property constraints, property and process models, as well as an objective function are involved in a computer-aided IL design (CAILD) task. In this section, we first introduce the structural and property constraints for generating feasible IL candidates. The optimization-based CAILD problem is then formulated and the solution framework is introduced.

5.1. IL structural constraints

As indicated before, in total 59 IL building groups including 54 cation–anion groups and 5 substituent groups are involved in the property prediction models. These groups (denoted as group set G) are used as building blocks to generate IL candidates. The maximal number of occurrence of the substituent groups CH_3 , CH_2 , OCH_3 , OCH_2 and OH are set to 4, 12, 4, 4, and 4, respectively.

$$0 \leq n_{\text{CH}_3} \leq 4 \quad (43)$$

$$0 \leq n_{\text{CH}_2} \leq 12 \quad (44)$$

$$0 \leq n_{\text{OCH}_3} \leq 4 \quad (45)$$

$$0 \leq n_{\text{OCH}_2} \leq 4 \quad (46)$$

$$0 \leq n_{\text{OH}} \leq 4 \quad (47)$$

The 54 cation–anion groups are represented as group set CA . Eq. (48) ensures that only one cation–anion group is selected when building ILs.

$$\sum_{k \in \text{CA}} n_k = 1 \quad (48)$$

In total, 438,750 possible ILs can be generated when taking into account the above specifications on the maximal group

numbers. Additional constraints for composing reasonable IL structures are introduced below.

The octet rule is used to ensure that the generated molecules are structurally feasible [40].

$$\sum_{k \in G} (2 - v_k) n_k = 2 \quad (49)$$

where n_k represents the number of occurrence of group k in the IL molecule. v_k denotes the valence of group k . Table 1 classifies the 59 building groups according to their valences.

In addition to the structural feasibility rules, structural complexity constraints are also required to limit the complexity of generated molecules. In this work, two types of complexity constraints are considered. Four subsets of groups, ILV_1 , ILV_2 , ILV_3 , and ILV_4 , are first defined to represent the cation–anion groups with one, two, three, and four valences. When a one-valence cation–anion group is selected, the total number of groups in the IL molecule is restricted to six. When a two, three, or four-valence cation–anion group is selected, the allowed maximal number of groups are set to 7, 10, and 13, respectively.

$$\sum_{k \in G} n_k \leq 6 \text{ if } \sum_{k \in ILV_1} n_k = 1 \quad (50)$$

$$\sum_{k \in G} n_k \leq 7 \text{ if } \sum_{k \in ILV_2} n_k = 1 \quad (51)$$

$$\sum_{k \in G} n_k \leq 10 \text{ if } \sum_{k \in ILV_3} n_k = 1 \quad (52)$$

$$\sum_{k \in G} n_k \leq 13 \text{ if } \sum_{k \in ILV_4} n_k = 1 \quad (53)$$

Besides the above molecular size restrictions, the total number of oxygen-containing functional groups is limited to no more than two.

$$\sum_{k \in \{OCH_2, OCH_3, OH\}} n_k \leq 2 \quad (54)$$

5.2. IL property constraint

In order to make sure that the phase-change heat storage takes place in the TES process, the melting point of ILs must

be larger than the system initial temperature (323.15 K) and lower than the inlet water temperature (343.15 K).

$$323.15 \text{ K} < T_m < 343.15 \text{ K} \quad (55)$$

5.3. Solution framework

The overall CAILD task is formulated as an optimization problem summarized as follows.

Maximize: Heat storage power: Eqs. (27) and (28)

Variable: Non-negative integer n_k ($k \in G$)

Subject to: Variable boundaries: Eqs. (43)–(48)

Structural and property constraints:

Structural feasibility rule: Eq. (49)

Structural complexity constraints: Eqs. (50)–(54)

IL property constraint: Eq. (55)

GC-based property models:

Latent heat: Eq. (30)

FC-CS equations: Eqs. (33)–(38)

Density: Eq. (39)

Heat capacity: Eq. (40)

Thermal conductivity: Eq. (41)

Melting point: Eq. (42)

Process models:

Heat transfer fluid: Eqs. (1)–(15)

PCM: Eqs. (16)–(26)

Due to the piecewise functions between IL enthalpy and temperature and the complexity in discretizing the PDEs into algebraic equations, it is difficult to solve the above CAILD problem using deterministic optimization methods. Therefore, in the present work, we choose to use the decomposition-based approach to solve the problem. The overall solution framework is illustrated in Fig. 6. As indicated, starting from the 59 IL building groups, 438,750 possible IL structures can be generated when taking into account the limitations on group numbers (Eqs. (43) – (48)). After discarding the structurally infeasible ILs using Eq. (49), this number is reduced to 20,930. The structural complexity constraints further cut down this number to 2370. Finally, 528 ILs are retained after imposing the melting point constraint. These 528 IL structures are used as input information for the property and process models to calculate their heat storage power. Consequently, a list of top ILs can be obtained.

Table 1

Classification of the 59 IL building groups according to their valences.

Valence of group	Group name
1	[CH ₃], [OCH ₃], [OH], [MIm][BF ₄], [MMPy][BF ₄], [Py][BF ₄], [NH ₃][BF ₄], [MIm][PF ₆], [MPyrro][PF ₆], [Py][PF ₆], [MPy][PF ₆], [MIm][Cl], [MPy][Cl], [MMIm][Cl], [MIm][Br], [MMIm][Br], [Py][Br], [MPyrro][Br], [MIm][NO ₃], [Py][NO ₃], [MIm][Tf ₂ N], [MMIm][Tf ₂ N], [Py][Tf ₂ N], [MPy][Tf ₂ N], [MPip][Tf ₂ N], [MPyrro][Tf ₂ N], [MIm][MeSO ₄], [MIm][O ₂ SO ₄], [MIm][TfO], [MMIm][TfO], [Py][TfO], [MPy][TfO], [MMPy][TfO], [MPip][TfO], [MIm][TOS], [MIm][I], [MMPy][I], [NH ₃][FOR], [MIm][TFA]
2	[CH ₂], [OCH ₂], [Im13][BF ₄], [NH ₂][BF ₄], [Im13][NO ₃], [Im13][Tf ₂ N]
3	[NH][BF ₄], [NH][PF ₆], [NH][MeSO ₃], [NH][TfO]
4	[N][BF ₄], [N][PF ₆], [P][PF ₆], [N][Cl], [N][Br], [N][NO ₃], [N][Tf ₂ N], [N][EtSO ₄], [N][MeSO ₃], [P][MeSO ₃]

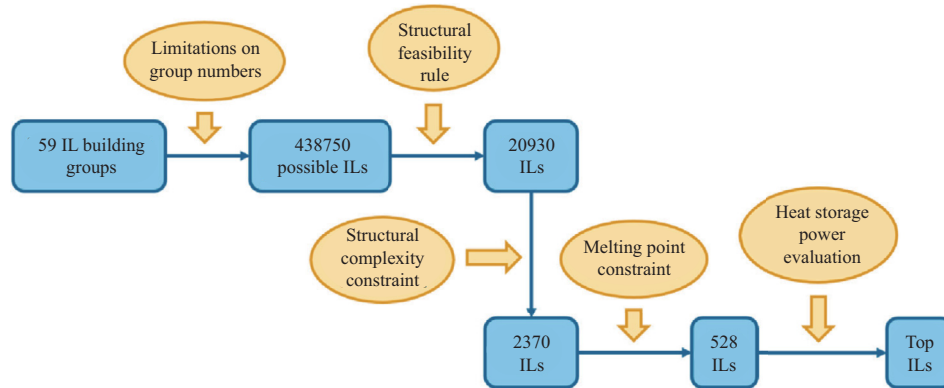


Fig. 6. Solution framework of the CAILD problem.

6. Results and discussion

As indicated by Eqs. (27) and (28), a total thermal charging time needs to be specified in order to determine the average TES power of a PCIL. In this work, we assume that the hot water is generated by solar radiation. According to Ref. [41], the German average sunshine duration in June is about 10 h per day. Therefore, the CAILD work is performed under 10 h thermal charging time. From the process model presented in Section 3.1, it is known that five thermo-physical properties of PCM including density, heat capacity, thermal conductivity, latent heat and melting point are required for evaluating the TES performance. In order to understand which properties are most influential, a parameter sensitivity study is performed. The average value of each property in the top 9 ILs identified from CAILD is used as the nominal value for this property. The allowed variation ranges for ρ , C_p , k and L are from 90% to 110% of their nominal values and for melting point, this range is from 323.15 K to 343.15 K. When studying the sensitivity of one property, the other properties are fixed at their nominal values. A sensitivity index function is defined to indicate the significance of the effect of a property on the thermal storage power, as shown in Eq. (56).

$$\text{Sensitivity} = \frac{POW_{upp} - POW_{low}}{pro_{upp} - pro_{low}} \quad (56)$$

where pro_{upp} and pro_{low} are the upper and lower bounds of a property. POW_{upp} and POW_{low} are the thermal storage power of the system determined at the upper and lower bounds of the property, respectively. Physically, the sensitivity of a property to the heat storage power is exactly the slope of the $POW-pro$ line. In some special cases when the slope changes substantially in the whole property region, more than one sensitivity values should be calculated and used. With the determined sensitivities, the superiority of a certain material over the other can be well interpreted through the comparison of the partial contributions of different properties on the TES power.

The top nine IL group combinations, physical properties and their corresponding TES power for the 10 h charging time are summarized in Table 2. The molecular structures of these ILs are plotted in Fig. 7. Additionally, the results of property sensitivity study are depicted in Fig. 8 where the detailed sensitivity value of each property is provided. As indicated in Fig. 8a, the average TES power of the system decreases as the melting point of ILs increases from 323.15 K to 343.15 K. For an IL with a low T_m , the temperature gradient on the solid–liquid interface (i.e., between outer-layer melted PCM and

Table 2
List of top 9 IL PCMs identified from CAILD.

Rank	Group combinations	POW (W)	T_m (K)	C_p (J kg ⁻¹ K ⁻¹)	ρ (kg m ⁻³)	L (J kg ⁻¹)	λ (W m ⁻¹ K ⁻¹)
1	2 CH ₂ , 1 OH, 1 [MPy][TfO]	4575.9	323.85	2171	1426	134,263	0.158
2	1 CH ₂ , 1 OH, 1 [MPy][TfO]	4513.6	327.61	2166	1474	137,321	0.162
3	2 CH ₂ , 1 OCH ₃ , 1 [MPy][TfO]	4501.9	323.99	1758	1333	151,571	0.152
4	1 CH ₂ , 1 OCH ₃ , 1 [MPy][TfO]	4440.3	327.75	1793	1374	155,325	0.156
5	1 OH, 1 [MPy][TfO]	3870.2	331.37	2146	1530	140,709	0.166
6	1 OCH ₂ , 1 CH ₃ , 1 [MPy][TfO]	3814.9	327.75	1793	1374	117,804	0.156
7	1 OCH ₃ , 1 [MPy][TfO]	3749.9	331.51	1811	1420	159,463	0.160
8	1 CH ₃ , 4 CH ₂ , 1 [MPy][TfO]	3733.4	326.94	1628	1264	130,595	0.149
9	1 OCH ₃ , 1 [MIm][NO ₃]	3716.0	329.45	1499	1261	134,122	0.204
BM	Paraffin Wax # 60	3160.5	333.05	2150	850	190,000	0.230

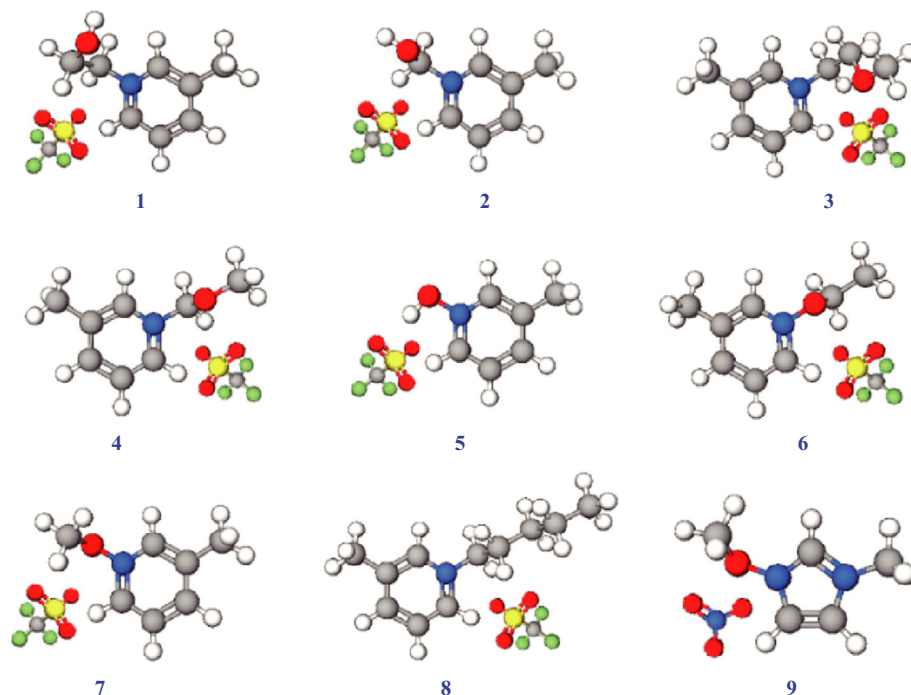


Fig. 7. Molecular structures of the top nine ILs.

the inner-layer melting PCM) is large. This makes the latent heat absorption faster and consequently leads to a higher thermal storage power. Except melting point, all the other four properties show positive effects on the TES power (see Fig. 8b–e). The reason can be easily understood from the physical knowledge on the system or directly from the process models.

As indicated in Table 2, all of the top nine ILs show a substantially higher TES power than the benchmark (BM) material paraffin wax # 60. Comparing these ILs with the wax, we find that the influence or contribution of heat capacity and thermal conductivity on the thermal power (indicated by the size of the product of property difference and sensitivity) are much smaller compared to the other three properties. Even though the wax has a higher latent heat that increases the thermal power, its higher melting point (note T_m has a large negative effect) and the much smaller density make this material worse than the ILs.

[MPy][TfO] is found to be the most favorable IL group for maximizing the TES performance. When comparing the 7th and 9th ILs, it is found that [MPy][TfO] has large contributions to the density and latent heat, which makes this group more favorable than [MIm][NO₃] for the investigated TES task. Regarding the functional groups, OH and OCH₃ are highly beneficial for increasing the thermal power of ILs. OH is slightly better than OCH₃ when [MPy][TfO] is selected as the main group (comparing 1st *versus* 3rd IL, 2nd *versus* 4th IL, and 5th *versus* 7th IL). The reason is that even though OCH₃ contributes more to the latent heat, the OH group has larger contributions to both heat capacity and density. However, comparing the 9th IL [MIm-OCH₃][NO₃] with the 15th

IL [MIm-OH][NO₃], the opposite trend is observed. Note that the GC-predicted latent heat is in the molar basis and the latent heat used in the process model is in the mass basis. Due to the much smaller molecular weight of [MIm][NO₃] compared to [MPy][TfO], the superiority of OCH₃ on the mass-based latent heat becomes prominent when combined with the [MIm][NO₃] group.

Comparing the 1st, 2nd, and 5th ILs or 3rd, 4th, and 7th ILs, we find that two CH₂ groups are most beneficial for the thermal storage. Table 3 shows the five properties and TES power of the ILs [MPy(CH₂)_nOH][TfO] and [MPy(CH₂)_nOCH₃][TfO] with different alkyl chain lengths. As indicated, increasing the alkyl chain lengths from 0 CH₂ to 2 CH₂ results in a much lower melting point, which finally leads to a higher thermal power due to the large negative effect of T_m . To further increase the number of CH₂ group makes T_m lower than 323.15 K, which leads to a significantly lower TES power due to the absence of LHS contribution (note that the initial temperature of the PCM is 323.15 K). When looking at the 8th IL that is connected with pure alkyl substituent, we find that long chains are preferred in this case. Note that due to the limitation on IL molecular size, the number of CH₂ group cannot exceed four in this case. Table 4 illustrates the influence of alkyl chain length on the thermal storage power of [MPy(CH₂)_nCH₃][TfO] ($0 \leq n \leq 4$). Through the analysis of the property sensitivity and contribution to the thermal power, it can be found that the effect of T_m is still the dominant factor in this case. The melting point of [MPy(CH₂)₄CH₃][TfO] is lowest among the 5 ILs and still higher than 323.15 K. Therefore, it shows the largest TES power.

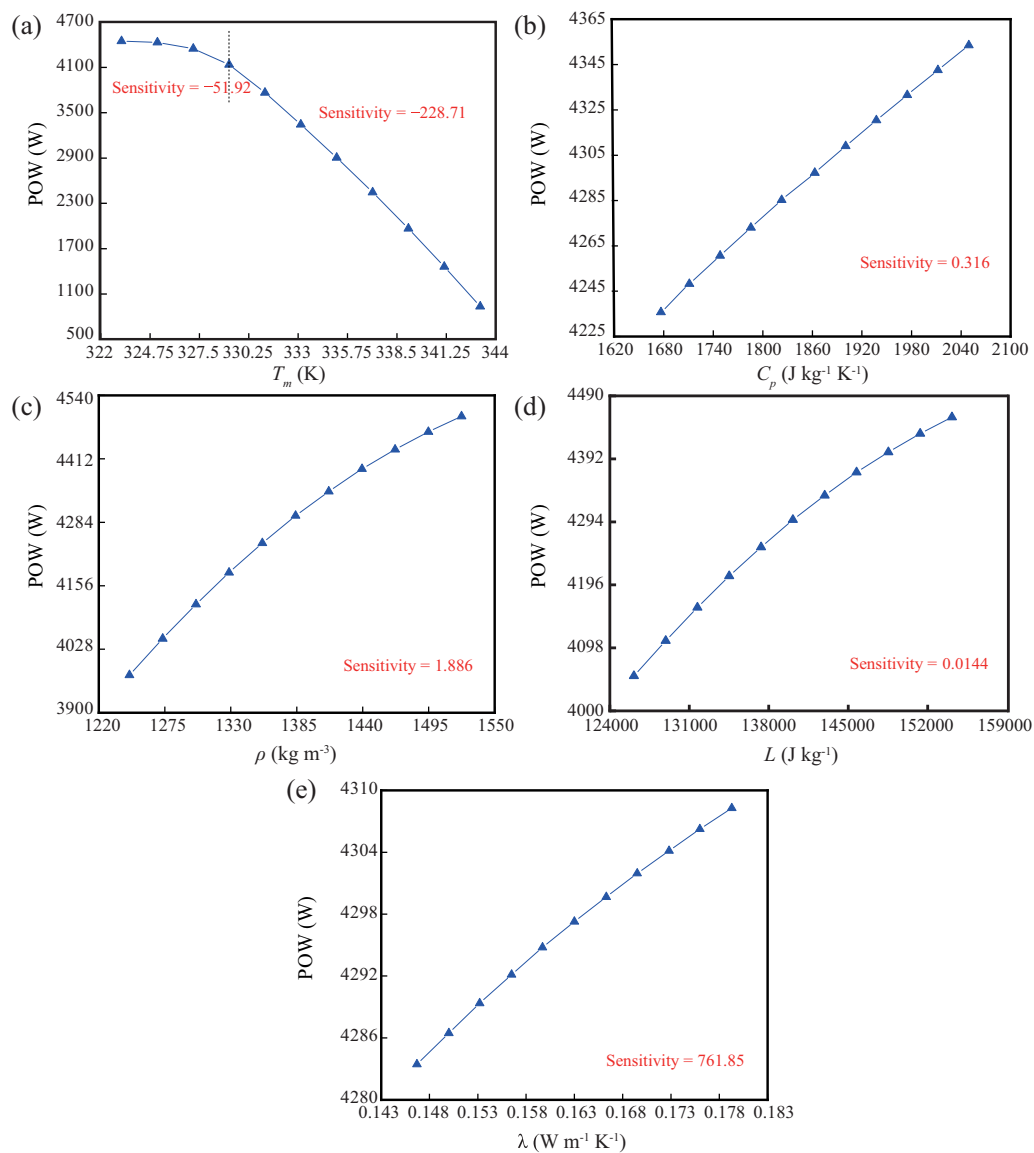


Fig. 8. Dependence of TES power on the melting point (a), heat capacity (b), density (c), latent heat (d), and thermal conductivity (e) of ILs.

Table 3

Influence of alkyl chain length on the TES power of $[MPy(CH_2)_nOH][TfO]$ and $[MPy(CH_2)_nOCH_3][TfO]$ ($0 \leq n \leq 4$).

Group combinations	POW (W)	T_m (K)	C_p ($J\ kg^{-1}\ K^{-1}$)	ρ ($kg\ m^{-3}$)	L ($J\ kg^{-1}$)	λ ($W\ m^{-1}\ K^{-1}$)
1 OH, 1 [MPy][TfO]	3870.2	331.37	2146	1530	140,709	0.166
1 CH ₂ , 1 OH, 1 [MPy][TfO]	4513.6	327.61	2166	1474	137,321	0.162
2 CH ₂ , 1 OH, 1 [MPy][TfO]	4575.9	323.85	2171	1426	134,263	0.158
3 CH ₂ , 1 OH, 1 [MPy][TfO]	1081.8	320.09	2159	1383	131,490	0.154
4 CH ₂ , 1 OH, 1 [MPy][TfO]	1038.5	316.33	2131	1345	128,964	0.150
1 OCH ₃ , 1 [MPy][TfO]	3749.9	331.51	1811	1420	159,463	0.160
1 CH ₂ , 1 OCH ₃ , 1 [MPy][TfO]	4440.3	327.75	1793	1374	155,325	0.156
2 CH ₂ , 1 OCH ₃ , 1 [MPy][TfO]	4501.9	323.99	1758	1333	151,571	0.152
3 CH ₂ , 1 OCH ₃ , 1 [MPy][TfO]	800.9	320.23	1705	1297	148,151	0.149
4 CH ₂ , 1 OCH ₃ , 1 [MPy][TfO]	747.6	316.47	1632	1265	145,023	0.145

Table 4
Influence of chain length on the TES power of [MPy(CH₂)_nCH₃][TfO] (0 ≤ n ≤ 4).

Group combinations	POW (W)	T _m (K)	C _p (J kg ⁻¹ K ⁻¹)	ρ (kg m ⁻³)	L (J kg ⁻¹)	λ (W m ⁻¹ K ⁻¹)
1 CH ₃ , 1 [MPy][TfO]	1211.8	341.98	1746	1425	142,786	0.166
1 CH ₂ , 1 CH ₃ , 1 [MPy][TfO]	2143.1	338.22	1741	1376	139,266	0.161
2 CH ₂ , 1 CH ₃ , 1 [MPy][TfO]	2983.0	334.46	1720	1334	136,091	0.157
3 CH ₂ , 1 CH ₃ , 1 [MPy][TfO]	3688.7	330.70	1683	1297	133,214	0.153
4 CH ₂ , 1 CH ₃ , 1 [MPy][TfO]	3733.4	326.94	1628	1264	130,595	0.149

7. Conclusions

Although ILs are extensively studied as reaction media [42,43] and separation solvents [44,45], there is an emerging interest in using this type of material for thermal energy storage. As summarized in Van Valkenburg et al. [46], the properties where ILs compare favorably with organic TES materials are thermal stability, density, heat capacity, vapor pressure and adjustable melting point. The property where ILs compare unfavorably is their high cost. Optimistically, although ILs are currently expensive, the ever-increasing interest and demand for large-scale industrial uses will constantly drive their cost to decrease.

To the best of our knowledge, this work is one of the first attempts to systematically design PCILs for a real TES process. The effects of multiple IL properties on the TES performance are simultaneously captured in the process models and the optimal IL structures best compromising all the properties are found by solving a formulated CAILD problem. Excitingly, the identified ILs are demonstrated to be better than the conventional PCM in terms of the average TES power of the investigated system. It is proven in this work that PCILs are promising TES materials for medium-low temperature applications. Considering the non-volatility and large heat capacity of ILs, these materials are also favourable for high-temperature heat storage, e.g., concentrating solar power generation.

The decomposition-based instead of optimization method is used to solve the formulated CAILD problem. Because the entire design space is explored, global optimality of the solution can thus be ensured. However, the limitation of this solution strategy should not be neglected. For problems with large molecular design space and those involving process optimization, this method can be inefficient and computationally expensive.

Conflict of interest

The authors declare that they have no known competing financial interests or personal relationships that could have appeared to influence the work reported in this paper.

Acknowledgement

The authors acknowledge the financial support from Max Planck Society, Germany, for the Computer-Aided Material and Process Design (CAMPD) project.

Appendix A. Supplementary data

Supplementary data to this article can be found online at <https://doi.org/10.1016/j.gee.2020.12.017>.

References

- [1] A. Abhat, Sol. Energy 30 (1983) 313–332.
- [2] H. Mehling, L.F. Cabeza, Heat and Cold Storage with PCM, Springer, Berlin, 2008.
- [3] J. Belman-Flores, J. Barroso-Maldonado, A. Rodríguez-Muñoz, G. Camacho-Vázquez, Renew. Sustain. Energy Rev. 51 (2015) 955–968.
- [4] S. Seddegh, X. Wang, A.D. Henderson, Z. Xing, Renew. Sustain. Energy Rev. 49 (2015) 517–533.
- [5] D. Aydin, S.P. Casey, S. Riffat, Renew. Sustain. Energy Rev. 41 (2015) 356–367.
- [6] C.Y. Fang, F. Tang, L. Cao, Renew. Sustain. Energy Rev. 40 (2014) 237–259.
- [7] A. Sharma, V.V. Tyagi, C.R. Chen, D. Buddhi, Renew. Sustain. Energy Rev. 13 (2009) 318–345.
- [8] R.K. Sharma, P. Ganesan, V.V. Tyagi, H.S.C. Metselaar, S.C. Sandaran, Energy Convers. Manag. 95 (2015) 193–228.
- [9] M. Kenisarin, K. Mahkamov, Renew. Sustain. Energy Rev. 11 (2007) 1913–1965.
- [10] Z.B. Zhou, H. Matsumoto, K. Tatsumi, Chem. Eur. J. 12 (2006) 2196–2212.
- [11] T. Zhou, L. Chen, Y. Ye, L. Chen, Z. Qi, H. Freund, K. Sundmacher, Ind. Eng. Chem. Res. 51 (2012) 6256–6264.
- [12] Z. Song, H. Shi, X. Zhang, T. Zhou, Chem. Eng. Sci. 223 (2020) 115752.
- [13] X. Kang, Z. Chen, Y. Zhao, J. Hazard Mater. 397 (2020) 122761.
- [14] X. Kang, X. Liu, J. Li, Y. Zhao, H. Zhang, Ind. Eng. Chem. Res. 57 (2018) 16989–16994.
- [15] L. Jiang, K. Mei, K. Chen, R. Dao, H. Li, C. Wang, Green Energy Environ. (2020) doi:10.1016/j.gee.2020.08.008.
- [16] H. Watanabe, T. Komura, R. Matsumoto, K. Ito, H. Nakayama, T. Nokami, T. Itoh, Green Energy Environ. 4 (2019) 139–145.
- [17] N. Terasawa, S. Tsuzuki, T. Umecky, Y. Saito, H. Matsumoto, Chem. Commun. 46 (2010) 1730–1732.
- [18] J. Zhu, L. Bai, B. Chen, W. Fei, Chem. Eng. J. 147 (2009) 58–62.
- [19] R. Vijayraghavan, U.A. Rana, G.D. Elliott, D.R. Macfarlane, Energy Technol. 1 (2013) 609–612.
- [20] N.V. Plechkova, K.R. Seddon, Chem. Soc. Rev. 37 (2008) 123–150.
- [21] Z. Song, X. Li, H. Chao, F. Mo, T. Zhou, H. Cheng, L. Chen, Z. Qi, Green Energy Environ. 4 (2019) 154–165.
- [22] Z. Song, C.Y. Zhang, Z.W. Qi, T. Zhou, K. Sundmacher, AIChE J. 64 (2018) 1013–1025.
- [23] T. Zhou, Z. Song, X. Zhang, R. Gani, K. Sundmacher, Ind. Eng. Chem. Res. 58 (2019) 5777–5786.
- [24] T. Zhou, H. Shi, X. Ding, Y. Zhou, Chem. Eng. Sci. 229 (2021) 116076.
- [25] A.F. Regin, S.C. Solanki, J.S. Saini, Renew. Energy 34 (2009) 1765–1773.
- [26] P. Galione, O. Lehmkuhl Barba, J. Rigola Serrano, A. Oliva Llana, I.M. Rodríguez Pérez, ISES Solar World Congress, 2011, pp. 1–12.
- [27] N. Wakao, S. Kaguei, T. Funazkri, Chem. Eng. Sci. 34 (1979) 325–336.
- [28] K. Vafai, M. Sozen, J. Heat Tran. 112 (1990) 690–699.

- [29] Ionic Liquids Database - ILThermo (v2.0). <https://ilthermo.boulder.nist.gov/>, 2020. (Accessed 15 July 2020).
- [30] Y. Huang, H. Dong, X. Zhang, C. Li, S. Zhang, *AIChE J.* 59 (2013) 1348–1359.
- [31] J.A. Lazzús, *Ind. Eng. Chem. Res.* 48 (2009) 8760–8766.
- [32] A. Mehrkesh, A.T. Karunanithi, *Fluid Phase Equil.* 427 (2016) 498–503.
- [33] J.A. Lazzús, *Fluid Phase Equil.* 313 (2012) 1–6.
- [34] L.M. Chávez-Islas, R. Vasquez-Medrano, A. Flores-Tlacuahuac, *Ind. Eng. Chem. Res.* 50 (2011) 5153–5168.
- [35] F.K. Chong, V. Andiappan, D.K.S. Ng, D.C.Y. Foo, F.T. Eljack, M. Atilhan, N.G. Chemmangattuvalappil, *ACS Sustain. Chem. Eng.* 5 (2017) 5241–5252.
- [36] F.K. Chong, D.C.Y. Foo, F.T. Eljack, M. Atilhan, N.G. Chemmangattuvalappil, *Mol. Syst. Des. Eng.* 1 (2016) 109–121.
- [37] A.T. Karunanithi, A. Mehrkesh, *AIChE J.* 59 (2013) 4627–4640.
- [38] B.C. Roughton, B. Christian, J. White, K.V. Camarda, R. Gani, *Comput. Chem. Eng.* 42 (2012) 248–262.
- [39] D. Valencia-Marquez, A. Flores-Tlacuahuac, R. Vasquez-Medrano, *Ind. Eng. Chem. Res.* 51 (2012) 5866–5880.
- [40] N.D. Austin, N.V. Sahinidis, D.W. Trahan, *Chem. Eng. Res. Des.* 116 (2016) 2–26.
- [41] Statista, Average monthly sunshine hours in Germany. <https://www.statista.com/statistics/982758/average-sunshine-hours-germany/>, 2020. (Accessed 8 August 2020).
- [42] F. Rajabi, C. Wilhelm, W.R. Thiel, *Green Chem.* 22 (2020) 4438–4444.
- [43] Q. Zeng, Z. Song, H. Qin, H. Cheng, L. Chen, M. Pan, Y. Heng, Z. Qi, *Catal. Today* 339 (2020) 113–119.
- [44] Z. Song, X. Hu, Y. Zhou, T. Zhou, Z. Qi, K. Sundmacher, *AIChE J.* 65 (2019) e16625.
- [45] Z. Song, T. Zhou, Z. Qi, K. Sundmacher, *ACS Sustain. Chem. Eng.* 5 (2017) 3382–3389.
- [46] M.E. van Valkenburg, R. Vaughn, M. Williams, J. Wilkes, *Electrochem. Soc. Proc* 19 (2002) 112–123.